

Evaluation of 3D small-scale lithological heterogeneities and pore distribution of the Boda Claystone Formation using X-ray computed tomography images (CT)

Saja M. Abutaha¹, János Geiger¹, Sándor Gulyás¹ and Ferenc Fedor²

¹ University of Szeged, Department of Geology and Paleontology; 6722, Szeged, Egyetem utca 2-6, Hungary; (sajaabutaha@geo.u-szeged.hu, matska@geo.u-szeged.hu, gulyas.sandor@geo.u-szeged.hu).

² GEOCHEM Ltd, 55/1 Viola str., Kozármisleny, H-7761, Hungary; (fedor.ferenc@geochem-ltd.eu)

doi: 10.4154/gc.2021.17



Abstract

This study was undertaken to quantify and evaluate the density and porosity characteristics of a Boda Claystone Formation (BCF) core sample using medical CT. Each voxel of the 3D CT volume was described with three variables: dry CT number, saturated CT number, and effective porosity. Disparity pore voxels were revealed using the genetic groups' algorithm of data-mining techniques. The K-fold cross-validation algorithm has been applied to determine the number of the most stable cluster. The 3D spatial distributions of voxel-porosity by rock constituents, as well as the 3D distribution of porosity clusters by rock components, were found by Boolean function implementation.

The terrigenous detrital fragments had the lowest porosity mean (0.16%) and highest coefficient variation value (1039.39%). While the Fine siltstone component had the highest porosity mean (3.39%) and lower coefficient of variation (134.99%). The difference in the variation of coefficient proportions is related to the outlier ratios in each rock component.

Independently of both the rock types and the sedimentary structures, two clusters could be defined: one for the micro-porosity and one for the macro-porosity regimes. The former showed a continuous 3D spatial appearance, while the latter appeared in patches. These patches may also be connected, at least partly, to some local smectite aggregates. These clay minerals could lose their structured water content during vacuuming and swell when adsorbing water during sample saturation. In each rock type, the micro-porosity regime could be related to low-density rock fragments. The mean effective porosity of the micro-pore regime was about 0.02, which corresponds to the petrophysical core measurements. For the macro regimes, the average was 0.1

Article history:

Manuscript received December 12, 2020

Revised manuscript accepted July 05, 2021

Available online October 13, 2021

Keywords: Boda Claystone Formation, CT, data mining, Boolean function, authigenic mineral

1. INTRODUCTION

Since its invention in the 1970s, X-ray computed tomography (CT) has spread and developed quickly, mostly stimulated by growing medical needs for diagnostic procedures and interventions. This technique which was initially meant to provide high-resolution non-destructive 3D reconstructions of bones and soft tissues, eventually attracted interest from other domains such as industry and the geosciences (e.g., GARVEY & HANLON, 2002; LOUIS et al., 2007). Although computerized X-ray tomography (CT or CAT scanning) has been used in the medical field for more than two decades (HOUNSFIELD, 1973; LEDLEY et al., 1974), recently, it has been widely adopted in studying earth system processes such as earthquakes, orogeny, basin tectonics, or fluid circulation involving mechanisms down to the scale of individual grains (micrometre–millimetre). The ability of X-ray CT to monitor these mechanisms non-destructively and in three dimensions in the laboratory makes it an ideal tool for geoscientists (SUTTON et al., 2002). The X-ray CT has been used in different fields of geosciences, such as studying microstructural and rock physical properties of geological media, aiding and enhancing production in petroleum geology or assessing soil contamination or waste repository issues in environmental geology (VAN KAICK & DELORME 2005; CNUDDÉ et al. 2006).

CT enables the analysis of the interior features of core samples, including bedding features, sedimentary structures, natural

and coring-induced fractures, cement distribution, small-scale grain size variation, and density variation (COLES et al., 1991; ORSI et al., 1994; COLES et al., 1998). This method has a wide application in geosciences, including analyses of the complex porosity and pore geometry of carbonate reservoirs (PURCELL et al., 2009), rock-fluid analysis (PYRAKNOLTE et al., 1997; PURCELL et al., 2009; WENBERG et al., 2009), the performance of diverting agents in unconsolidated sandstones (VINEGAR AND WELLINGTON, 1987; WELLINGTON & VINEGAR, 1987; RIBEIRO et al., 2007A), and many other topics. For instance, BONNER et al. (1994) confirmed fluid migration in rocks by X-ray CT. VERHELST et al. (1995), GEIGER et al. (2009) applied the technique to characterize small-scale heterogeneities in intact samples. SCHWARTZ et al. (1994) modeled the fluid flow in porous rocks by combining theoretical simulations with 3D imaging of the material studied. Additionally, according to the considered rock type, accurate permeability and conductivity estimations are possible using CT (FREDRICH et al. 1993; COKER et al. 1996; COLES et al. 1998; ARNS et al. 2001, 2004).

Micro-CT (μ CT) systems offer a new depth of information that has not been available with conventional two-dimensional microscopy analysis. Several studies have investigated the application of μ CT in mineral characterization, including pore analysis (YANG et al., 1984; VINEGAR AND WELLINGTON, 1987; WITHJACK, 1987; HOVE et al., 1988; SPRUNT et al., 1991),

liberation and grain exposure (COLES ET AL., 1991; SPANNE & RIVERS, 1987; NICHOLS et al., 1989; JONES et al., 1991; LONTOC-ROY et al., 2005; NAHMANI et al., 2005), crack and breakage analysis (CONNER et al., 1990; FLANNERY et al., 1987), as well as mineral segmentation analysis (e.g., FLANNERY et al., 1987). The main challenge in the full adoption of a μ CT system in these studies lies in the demanding computational processing of a large 3D dataset. Additionally, since most of the μ CT analyses are based on the attenuation of the minerals, the presence of minerals with similar attenuations limits the capability of μ CT in mineral segmentation (GUNTORO et al., 2019). So, although the resolution of a medical CT is much lower than that of the μ CT, correspondence between the scales of medical CT measurements and petrophysical, sedimentological measurements applied to core samples makes it better suited for general core sample investigations (GEIGER et al., 2009).

The present study focuses on quantifying and evaluating density and porosity characteristics of a core sample using medical CT scans at the scale of a hand-size specimen. A porosity dataset is derived for the identified depositional units from two CT scans at the same location, dry and saturated. This dataset provides porosity information at a much higher resolution, the scale of voxels, compared to traditional petrophysical measurements yielding data for the entire sample as a whole. Coupled processing of information on rock-forming components with pore volume percentages on the same volume (Voxel) has a major advantage over traditional petrophysical approaches. This approach makes a straight connection between the presence and share of rock-forming components and the expected variances of petrophysical properties. Specific objectives could be addressed as follows: i) Identification of the rock-forming components in the studied CT volumes. ii) calculation of the voxel porosity of the rock-type constituents. iii) analysis and visualisation of the 3D voxel porosity values for each rock component. iv) classification of the voxels into the optimal number of clusters where each cluster has a unique 3D pattern. v) analysis and visualisation of the 3D clusters of voxel-porosity for each rock type. vi) comparison of the mean voxel-porosity with other conventional porosity measurements.

2. CT PRINCIPALS AND THE CT TECHNIQUE APPLIED

2.1. CT principals

The theoretical foundations of computed tomography (CT) were established by Cormack and Hounsfield (1989). Further technical developments in CT technology led to the introduction of new instruments ranging from spiral CT (1989), multi-slice CT, micro-CT, nano-CT (1998), to multi-slice CT with double X-ray tubes (GARVEY & HANLON 2002). The sample to be analyzed is placed within a gantry. X-ray radiation is transmitted through the sample in all directions of the points of a circle. Gamma rays interact with the matter in four ways: Raleigh scattering, photoelectric effect, Compton effect, and pair generation (SIEGBAHN, 1967). All these interactions are determined mainly by variations in the density and atomic composition of the highly collimated x-ray beam. Detectors on the opposite side of the core measure the intensity of the transmitted beam. The x-ray source and/or detectors rotate or translate around the sample. A series of x-ray attenuation measurements are numerically reconstructed to give the spatial distribution of x-ray attenuation coefficients within the sample. The image resolution depends on the thickness of the x-ray beam, the number of detectors in the scanner, and the pixel array size used to reconstruct the image. X-ray beam thickness

varies from about 2 mm to 10 mm. The CT measurements of geological samples enable the identification and evaluation of internal geological structures such as bedding planes, fractures and nodules, lithological changes, and bulk density. A combination of sequential x-y scans along the core axis can provide slab images or three-dimensional images of the core (ATTIX, 1986; KNOLL, 2000). If the transfer of energy is constant, X-rays' absorption depends only on the material they go through. For inhomogeneous samples including clastic sedimentary rocks, the attenuation coefficient has different values at different sample points (e.g., HOUNSFIELD, 1973, CURRY et al., 1990). The transmitted X-ray beam's intensity is usually expressed as the Hounsfield Unit (its synonym is the CT number).

Each Hounsfield unit (HU) represents a 0.1% change in density with respect to the calibration density scale. Water is assigned a value of 0 HU, with air being equal to (-1000) HU and maximum attenuating materials measuring near 3,000 HU. Images are then produced in a grayscale manner, with areas of low attenuation (low HU) being darker and high-attenuation regions (high HU) being brighter. With a given attenuation dataset, images can be further manipulated by changing the viewable window settings to accentuate specific contrast differences (WESOLOWSKI & LEV 2005; BOGNER et al. 2003; FÖLDES et al. 2004; FÖLDES 2011). Another essential feature of these types of analyses is the availability of a quantitative background dataset, which can be further evaluated both visually and by applying various statistical, or geostatistical approaches.

2.2. The CT technique applied

CT measurements of the 1 m-long core sample were performed on a Siemens Emotion 6 medical scanner at the Institute of Diagnostic Imaging and Radiation Oncology, University of Kaposvar, Hungary. The instrument operates at 120 kVp (peak kilovoltage), with 250 mAs (milliamperere-seconds) current, 1.0 s (sampling intervals). The lateral resolution was $0.1953 \times 0.1953 \text{ mm}^2$ with 1.25 mm of scan-layer thickness. The image reconstruction matrix was 512×512 pixels. The field of view (FOV) was approx. 9.99 cm. The cleared images were exported as DCOM images. This image format is a standard in medical applications and can be easily read by 'classical' 3D volume rendering software (e.g., VOXLER).

The method of voxel-scale porosity determinations using CT scans was introduced by WITHJACK (1988) and AKIN et al. (2000). At the University of Kaposvár, Földes, and his team introduced another dual-scanning approach for the evaluation of concrete elements (BALÁZS et al., 2018). They have measured this core material by the same methods. Firstly, they vacuumed the dry core material in a vacuuming tube. After six hours of vacuuming, they performed whole-core CT scans (dry condition). At the next step, they saturated the core material with water. After 1 hour of relaxation, they repeated the scanning process at the same position of the same measured slice (flooded or evacuated condition). They guaranteed that the Dicom files were free of any artifacts and that during the second scans they measured the sample pixels as during the first scan.

We have calculated the effective porosity values for each voxel of the scanned slices from both scans' datasets using the calculation suggested by MOSS et al. (1990).

3. THE GENERAL LITHOLOGICAL CHARACTERISTICS OF THE STUDY SAMPLE

Our study sample was taken from the Boda Claystone Formation (BCF). The Boda Claystone Formation represents the fill of a rela-

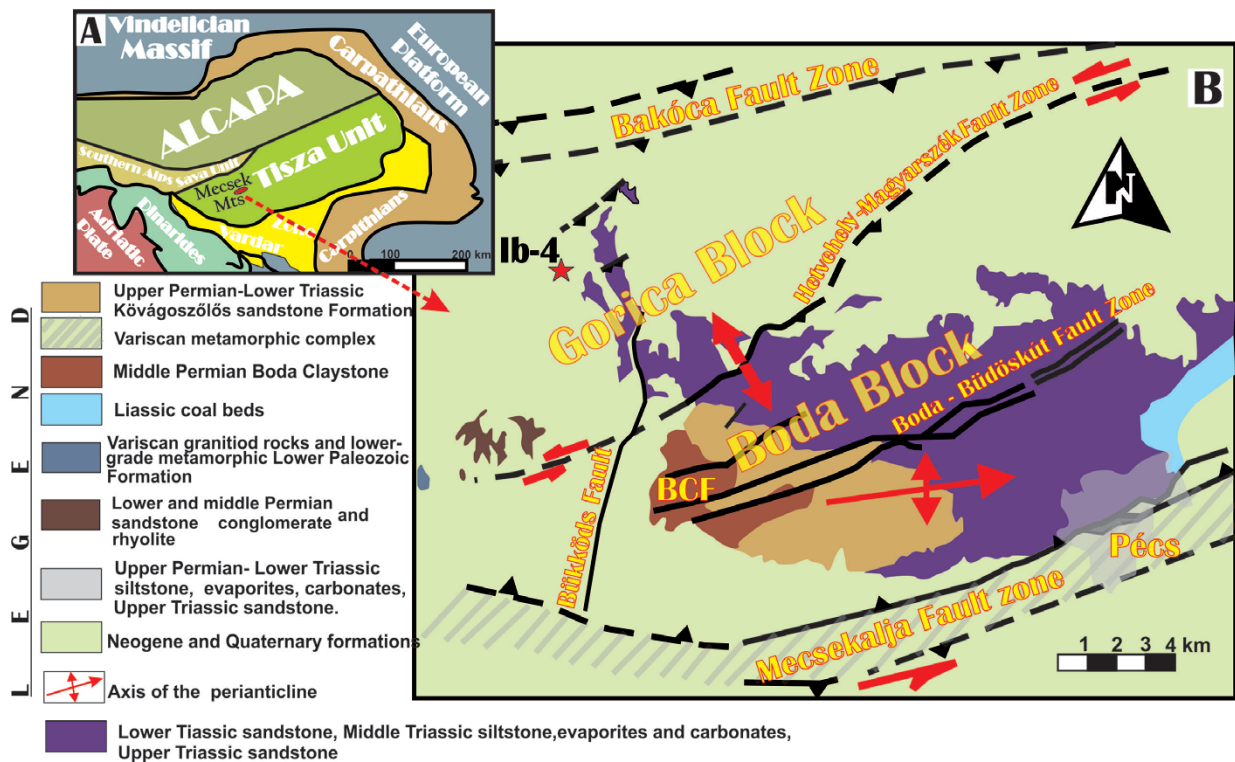


Figure 1 A: Distribution of the Boda Claystone Formation sequences in the Mecsek Hills area (after Haas & Péró, 2004; Konrad et al., 2010) with the location of the studied core site Ibafa 4 (Ib-4) marked by the red star at the left corner.

tively small, continuously subsiding basin, which was one of the continental strike-slip and rift-related basins in the northern part of the internal Variscan orogenic domain (VOZÁROVÁ et al., 2009). These Upper Permian terrestrial sequences are confined to the area of the Mecsek Hills in SW Hungary (Fig. 1A, HAAS & PÉRO 2004; CSONTOS & VÖRÖS, 2004). The BCF has two distribution areas in the Western Mecsek area: a perianticlinal structure and the so-called Gorica block (Fig. 1). Continental sedimentation in the Mecsek Mts. was initiated in the Early Permian and lasted until the early Triassic, yielding a 2000-4000m-thick continental clastic sequence (HAAS & PÉRO 2004). The transitional and playa sediments of the BCF occur within the Permian fluvial sequence.

The lithology of the Boda Claystone can generally be subdivided into three major units. It starts with fine-grained sandstone beds at the base, overlain by albitic claystone/siltstone, and then continues with claystone, albitic clayey siltstone, and silty claystone with dolomite at the top (KONRÁD, 1999).

Our study sample corresponds to a sample from the upper part of the Ibafa-4 core sequences encompassing the depth interval from 602.41 to 603.46 m (Fig. 2). At the request of GEOCHEM Ltd., with the approval of the Public Limited Company for Radioactive Waste Management (PURAM), as part of an R&D project, dry and flooded CT measurements of 0.89 m and 10.54 m on Ib-4 drill hole core material were carried out at the University of Kaposvár. The location and the detailed core profile description are shown in Figs. 1-2, respectively. In the referred sample, silty-claystone is the dominant rock component. Albitic nests, vertical burrows, fractures with calcite fill, lamination, and bioturbation are all reported in the core description.

Since 1998, the Public Limited Company for Radioactive Waste Management (PURAM), as a Hungarian governmental agency, has had the responsibility and monetary funds to coor-

dinate the studies on the Boda Claystone Formation as a potential high-level nuclear waste (HLW) disposal. In 2009, distinctive research was established to define intervals of CT numbers (HUs) corresponding to constituents of the BCF. As a result of the cooperation between the University of Szeged, GEOCHEM, and PURAM, the raw data sets were transferred to the University of Szeged for further scientific research. Defined CT intervals were as follows: Detrital fragments (Coarse siltstone): <2700 H.U, Fine siltstone: 2700-3150 HU, Claystone: 3150-3300 HU, Calcite and /or Dolomite: 3300-3600 H.U., and Albitic: >3600 HU. Current work has considered these intervals to identify the rock-forming components of the core sample.

4. THE GENERAL WORKFLOW OF ANALYSIS

All the CT scans were carefully processed to avoid artifacts such as beam hardening which occurs when the attenuation along a path passing through the centre of the object becomes larger than the attenuation along the path passing through the objects' marginal parts. This happens because lower-energy X-rays are attenuated more readily than higher-energy X-rays; a polychromatic beam passing through an object preferentially loses the lower-energy parts of its spectrum. The result is a beam that has higher average energy than the incident beam, though diminished in overall intensity. This also means that, as the beam passes through an object, the effective attenuation coefficient of any material diminishes, thus making short ray paths proportionally more attenuating than long ray paths. In X-ray CT images of sufficiently attenuating material, this process generally manifests itself as an artificial darkening at the centre of long ray paths and a corresponding brightening near the edges. Beam hardening can be a pernicious artifact because it changes the CT value of a material (or void) depending upon its location in an image. Thus, to

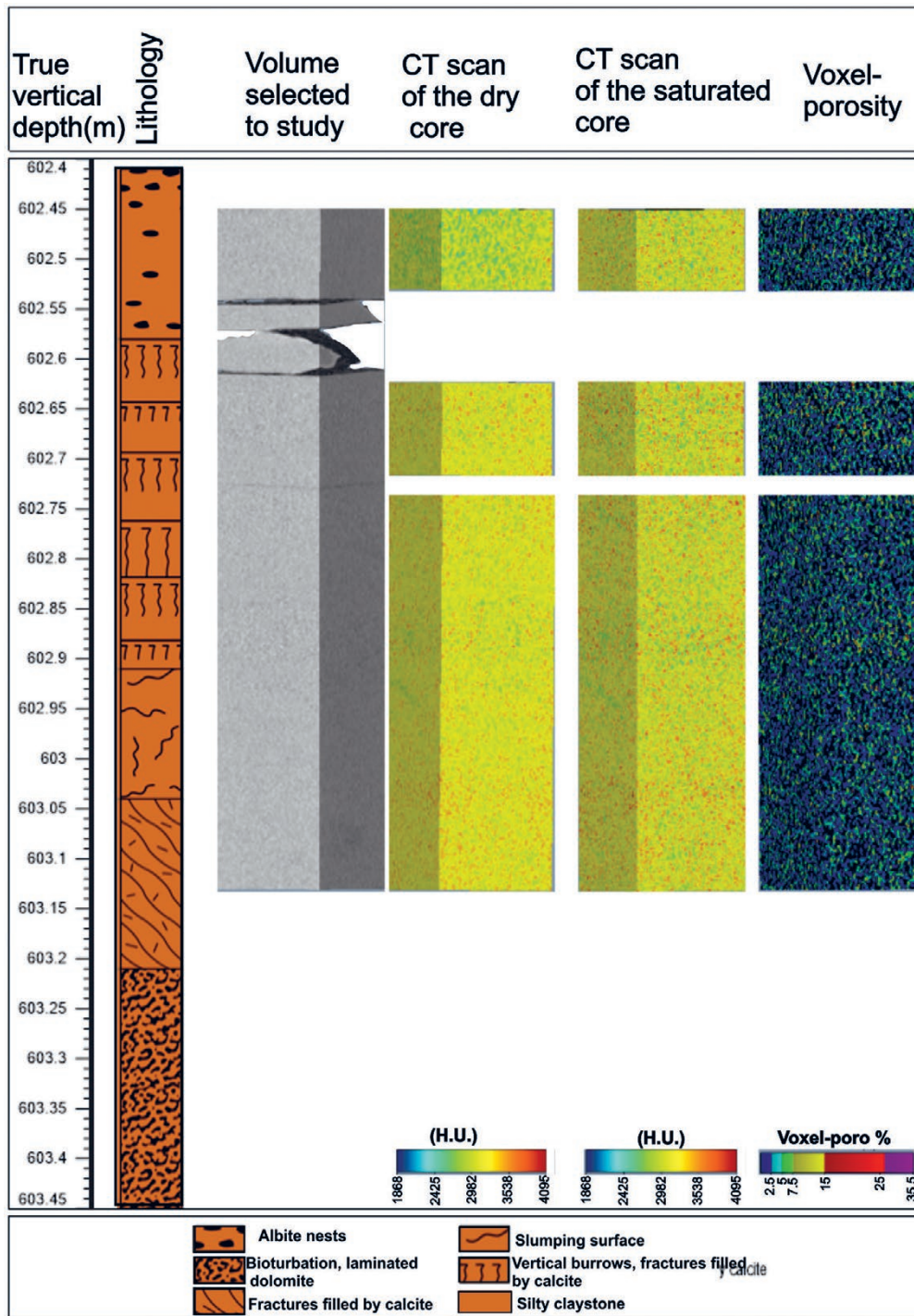


Figure 2. Rock column.

eliminate beam hardening, we remove the image's outer edges and analyze only the centre.

A 3D nearest neighbour algorithm was applied to build the 3D volumes of the scanned dry (vacuumed) and saturated core. This algorithm arranged the CT scans' grid systems below one another in the actual stratigraphic position and fully honoured the measured CT numbers. From the dual CT scans, three parameters were available in each voxel: CT number of the dry (vacuumed) state, CT number of the saturated state, and the calculated effective porosity (Fig. 2). The total number of voxels in each 3D model (dry core, saturated core, and effective porosity) was around 13 million.

The workflow applied in this study relied on three fundamental scopes. The first one was identifying rock constituents according to the pre-classified CT intervals taken from the PURAM project. In this calibration phase, the suggested CT intervals of the rock components were visually compared with the dry HU patterns of the 3D CT volume; definable geometric characteristics (i.e., sedimentary structures) were also detected ("Pre-Processing" in Fig.3).

Each voxel of the 3D CT volume was described with three variables: dry CT number, saturated CT number, and effective porosity. In our view, the dry and saturated CT numbers characterize the rock texture voxel by voxel, and the voxel porosity cal-

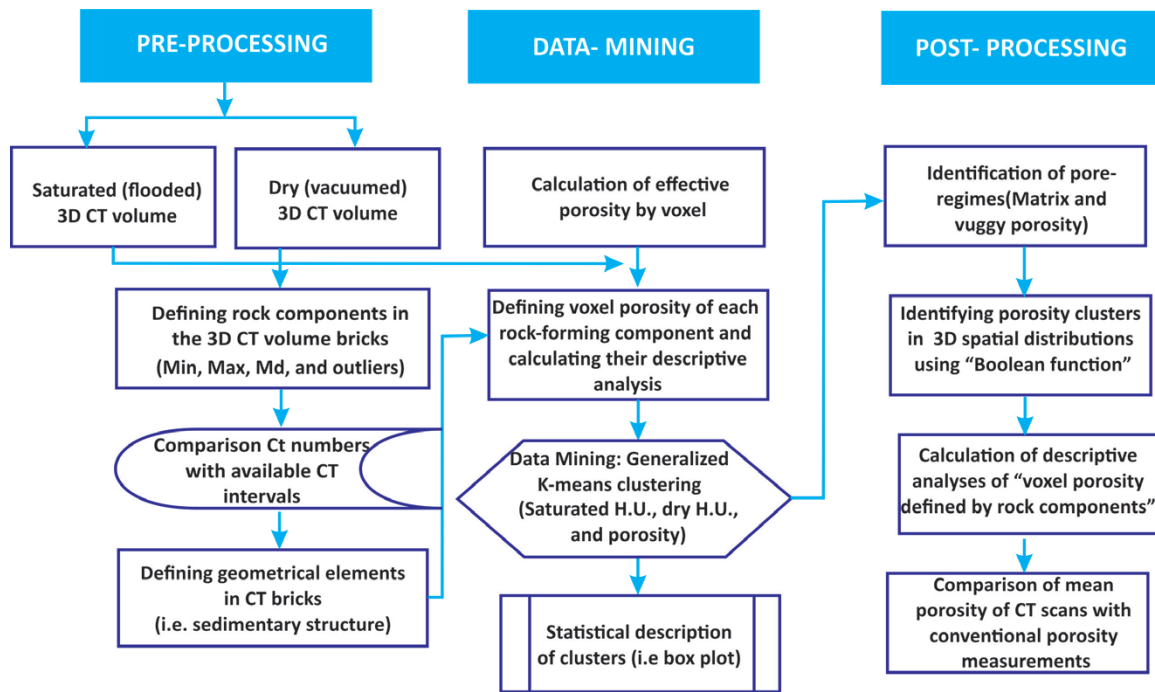


Figure 3. The workflow.

culated in each voxel describes the petrophysical characters of each voxel partially. The spatial patterns of the voxels with similar effective porosity and textural characters (dry and saturated CT numbers) were divulged by a generalized k-means clustering algorithm of data-mining techniques (“Data Mining” in Fig.3). In this process, we searched for the minimum number of “genetic groups”. Classifying CT numbers into the minimum k number of disjoint clusters is an iterative method that assigns each point to the cluster whose centroid is the nearest. Euclidean distance is generally considered to determine the distance between data points and the centroids. K-means clustering algorithm depends on the random choice of initial centroids. The computational complexity of K-means algorithms is very high, especially for large data sets. To determine the stable number of clusters, the K-fold cross-validation technique was used. Each time, one of the k subsets is used as the test set/ validation set, and the other k-1 subsets are put together to form a training set. The error estimation is averaged over all k trials to get the total effectiveness of our model. The recent approach significantly reduces bias as we are using most of the data for fitting which significantly reduces variance.

The final, third phase includes post-processing. The HU intervals of rock-type components coming from the first phase were used to build up the Boolean lattices for each textural component. These Boolean lattices were utilized to show the 3D spatial distributions of voxel-porosity by rock type (by multiplication of Boolean lattices with voxel porosity) and the 3D distribution of porosity clusters by rock components (by multiplication of Boolean lattices with clusters’ porosity).

Lastly, descriptive analyses were employed to estimate the statistical measure of central tendency and dispersion to organize the pores voxel information for each rock constituent in each HU 3D brick volume. A hypothesis test has been applied to evaluate and compare the implemented CT pore measurements with other conventional lab measurements, such as helium and mercury measurements.

5. RESULTS

5.1. CT characters of rock-forming components in the studied core

After the CT numbers calibration and clearing beam hardening, the intervals from PURAM’s study were linked with the actual geological information of the core sample to visualize the 3D rock-forming components distribution.

Each 3D brick of the dry scans includes 5 rock constituents (Fig. 4); detrital fragments shown as black (HU ≤2700), fine siltstone in grey (2700 HU-3150 HU), claystone with green (3150 HU-3300 HU), dolomite, and calcite cement appears in light orange (3300 HU-3600 HU), and Albite has a dark orange colour (HU>3600). A set of structures could also be identified, for instance; the upper first partition of the lithology profile in Fig. 4 shows albite nests; it appears in the first 3D volume brick. The vertical burrows and calcite-filled fractures are dominant throughout the second and upper third profile’s partitions. The middle part of the bottom lithological profile shows some slumping surfaces.

The bivariable histogram in Fig 5A shows both saturated and dry core HU frequency observations. The midst bins intervals of the fine siltstone and claystone components (2700-3300 HU) pointed out the higher dry HU observations than saturated ones. In contrast, the intervals corresponding to carbonate and albite nests (>3300 HU) are characterized by higher HU values of the saturated sample. The coarse siltstone intervals (2700-2400) display, again, greater HU frequency observations in the saturated than in the dry core.

Fig. 5B shows box-plot charts of the HU values for the dry and saturated core sample. The dry core’s median is around 3100, while the saturated one is slightly lower than this. The first quartile (lowest 25%) of dry and saturated HU values are similar, at about 3200. the third quartiles (75% mark) are 3250 and 3000 HU for the dry and saturated core samples, respectively. The HU saturated chart’s minimum value is 2550, and the maximum is 3700. Likewise, the minimum dry core HU value is 3175, and the maximum one is 3200. Plenty of high and low HU value outliers can

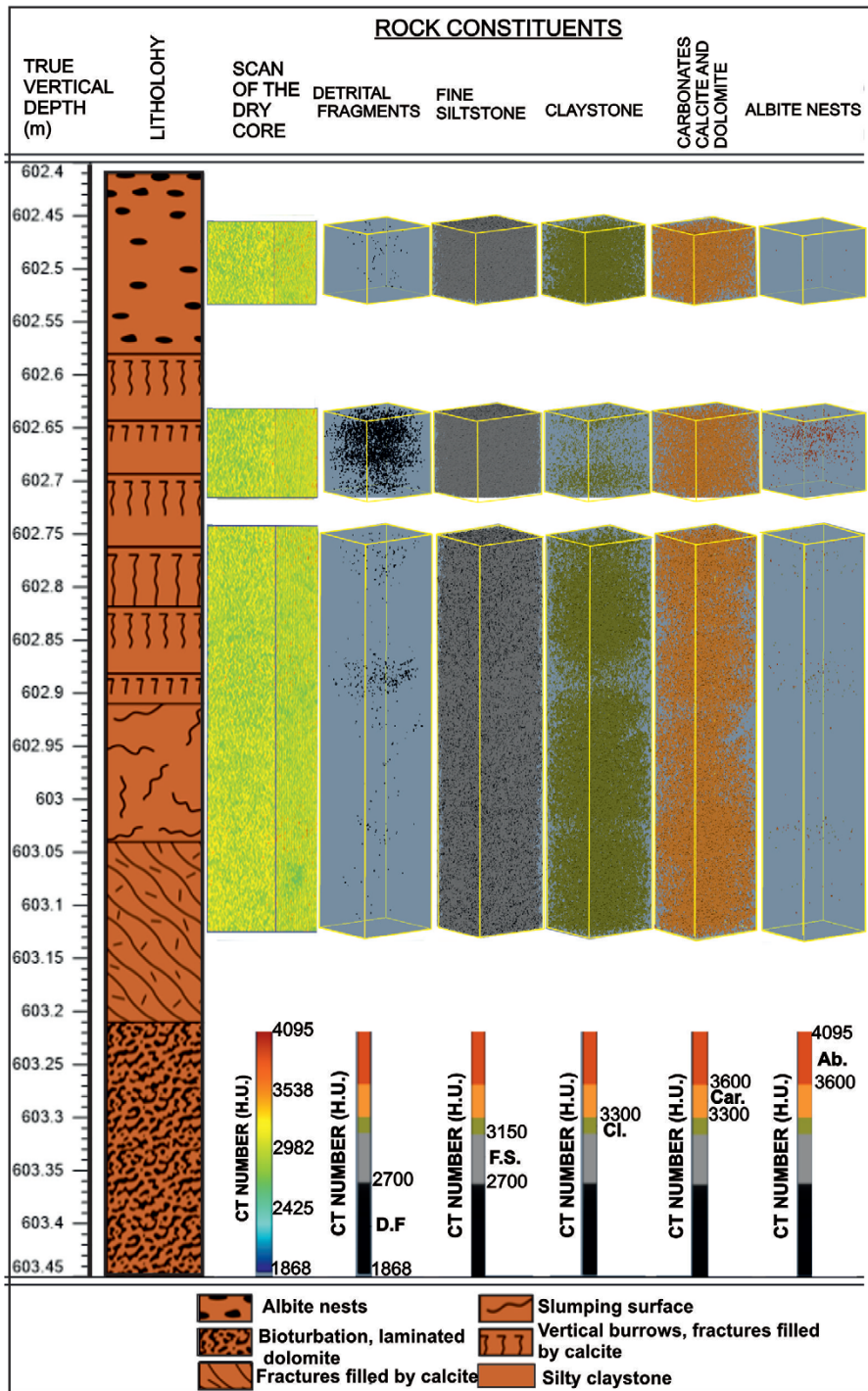


Figure 4. Rock-forming components. Legend; D.F.=Detrital fragments, F.S.=Fine siltstone, CL=Claystone, Car.=Carbonate and dolomite cement, Ab= Albite nests.

be found in the saturated core sample volume; however, no outliers have been noticed in the dry one. The increased height of the box of the HU saturated core volume indicates the greater variation dispersed data, while the decreased height of the HU dry volume box indicates the less dispersed data. As shown by the extreme outliers' values at the end of the two whiskers of the HU saturated core volume and the larger ranges, the overall spread indicates the wider distribution and more scattered points.

5.2. 3D spatial patterns within the core

The first 3D volume profile's bricks of the detrital fragments' porosity in Fig. 6, have 2881384 voxels; 21916 of these porosity values are greater than zero. The porosity mean of the terrigenous

detrital fragments is 0.16%, with a high coefficient of variation value reaching 1039.39%. However, the fine siltstone component has 8,006,806 of no null voxel porosity value from the overall voxels number (8,655,548). Its mean porosity is 3.39%, and the coefficient variation is 134.99%.

The claystone component includes 6238159 porosity voxels; 5540873 are not null (porosity values >0). The porosity voxels mean and the coefficient of variation of the claystone component is 1.10% and 1.21%, respectively.

The carbonate component consists of 4052229 voxels; 3500052 of the porosity voxels values are larger than zero. The mean of carbonate porosity voxel is 0.24%, with the second higher coefficient value of 458%.

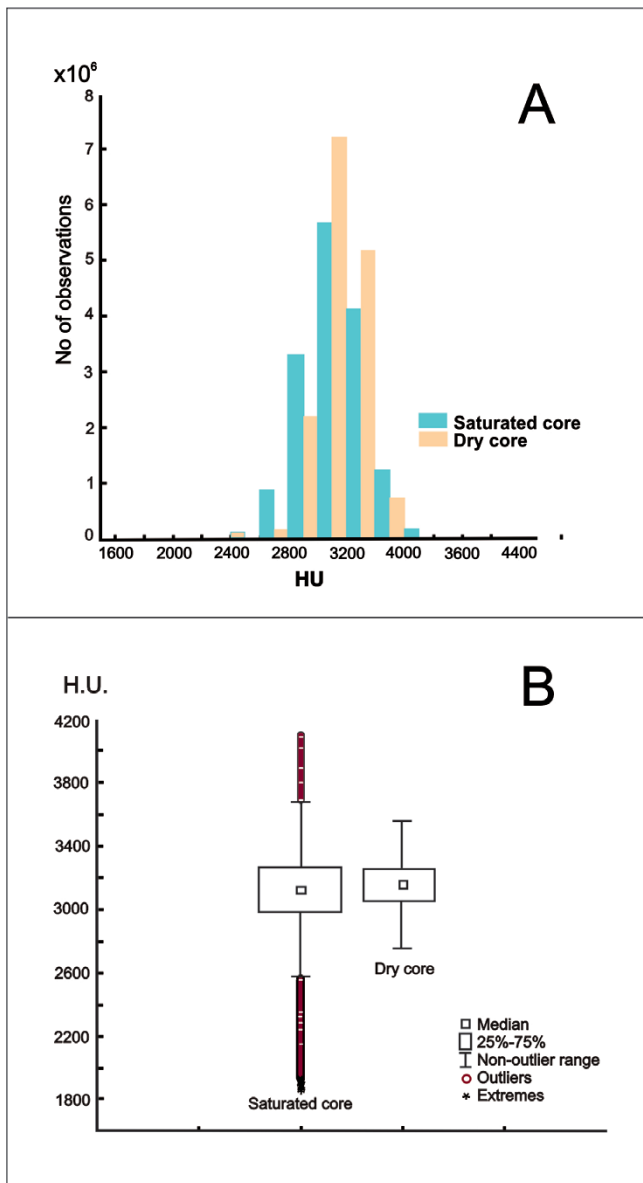


Figure 5. Histograms of the saturated and dry samples (A) and the corresponding box-plots (B)

The albite nests component has 2857049 voxels; only 177 of them have no null porosity values. The mean porosity voxels of the albite nests are 2.14%. And the coefficient of variation is 77.39%. Further details of porosity basic statistical properties by rock constituents are illustrated in Table 1.

The conspicuous sedimentary structures in the CT images; fractures, and convolute deformation are marked in Fig. 7A fracture in Fig. 7A shows high-density contrast between the calcite’s

infilling material and surrounding sediment. It is recognized as dark parts in the porosity CT image (Fig. 7B). Conversely, the convolute lamination textural pattern has almost been preserved in the CT porosity scan image (Fig. 7C-D).

Textural variables of the HU of the saturated core (FLD) and HU of the dry core, as well as the porosity variable for petrophysical properties, were utilized to detect textural and petrophysical voxel characteristics using the genetic groups’ technique. Our work deals with Chebyshev distances; 10 (v-value) cross-validation and 20 iterations were applied in each approximation. There were about 13 288 316 training cases (Fig. 8). The initial result of clustering was 6 clusters, k=6 (Fig. 8A). However, the arithmetic means of porosity manifest that Clusters 1, 3, and 6 are quite similar; clusters 5 and 2 are also comparable. Therefore, the maximum number of porosity clusters for the next run was suggested to be 3, and the minimum number of clusters premised to be 2, K=3 (Fig. 8B). Eventually, two clusters were demonstrated for genetic heterogeneity of the porosity values greater than zero, K=2 (Fig. 8C).

To compare the spread and centers of porosity values larger than zero for the two resultant clusters, the box-plot chart was used (Fig. 9).

The median of cluster 1 appears to be approximately 10%, whereas cluster 2 has a median of around 2.5%. 25% of cluster 1 porosity values are less than 8%. Hence, 75% of the porosity values in cluster 1 are larger than 8% and lower than 19% (IQR range=11%). In comparison, 25% of porosity values in cluster 2 are less than 1%. Thus, 75% of voxel porosity in cluster 2 is higher than 1% and lower than 8% (IQR range=7%). Therefore, the above two clusters could be presented by their average porosity values; matrix porosity with an average of 2.5%, and macro-pore porosity with a 10% average. The porosity outlier values beyond the upper whisker in Fig. 9, are an exclusive macro-pores cluster note. The outlier values are extended from 18% (over the maximum value) up to 37% (extreme outlier).

Fig. 10 shows the 3D distributions of the three porosity clusters for each rock constituent. Clusters are identified in three colours; black for no porosity, green for cluster 1 (Matrix porosity cluster), and cluster 2 has a red colour (macro-porosity cluster). The detrital fragments component shows almost a mixture of the three colours. The cluster of no porosity is prevalent in the fine siltstone component, while clusters 1 and cluster 2 are less abundant.

The pervasive cluster in the claystone component is the no-porosity cluster with the subdued appearance of cluster 1. Carbonate/dolomite and albite constituents show mostly no-porosity clusters.

The rock constituents ratios versus porosity clusters distribution are summarized in Fig. 11 which shows that each porosity cluster has different rock-forming components in definite ratios.

Table 1. Basic statistical properties of voxel porosity by rock constituents.

	No. of voxels	No. of No-null voxels	Mean of voxel porosity %	Md. Of voxel porosity %	Min. of voxel porosity %	Max. of voxel porosity %	Coefficient of variation %	Min. voxel porosity of outliers %
Rocks constituents								
Detrital fragments	2881384	21916	0.16	0.0006	0.0004	35.74	1039.39	32.33
Fine siltstone	8655548	8006806	3.39	0.52	0.0007	33.11	134.99	15.14
Claystone	6238159	5540873	1.1	0.0009	0.0005	23.08	221.12	1.21
Carbonate	4052229	3500052	0.24	0.0008	0.0006	19.24	457.34	2.10E-12
Albite nests	2857049	117	2.14	1.78	0.055	7.54	77.39	5.73

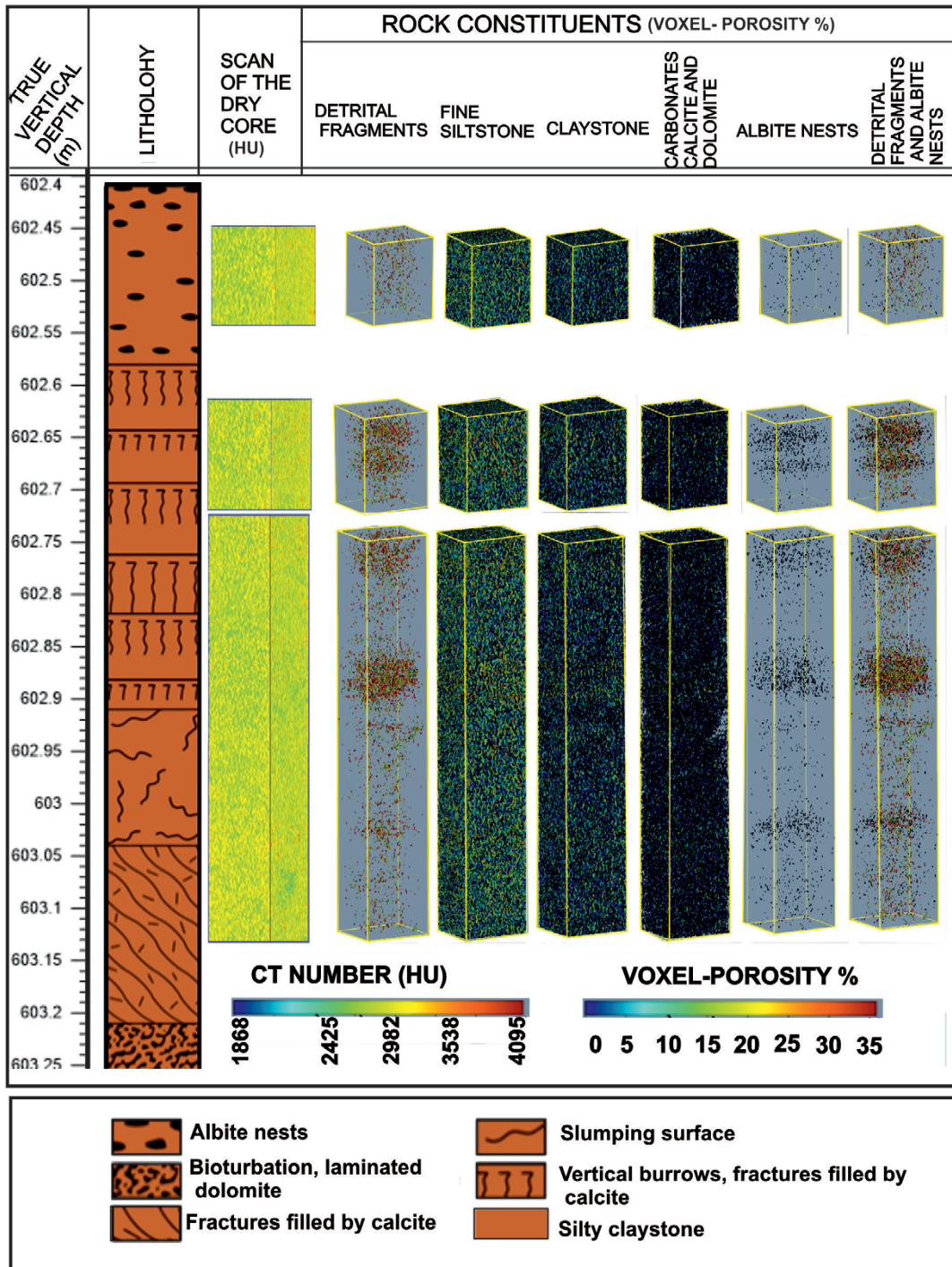


Figure 6. Porosity of the rock-forming components.

The no-porosity cluster shows a very dense texture, including a variety of rock components; it consists of about 19% fine siltstone, 23% Claystone, 13% carbonate, 0.16% albite, and is almost lacking detrital fragments. Compared with cluster 1, the fine siltstone forms around 20%, claystone is decreased to 8.44%. The carbonate content is also reduced to 1.66%, with no albite, and the detrital fragments component appears as 0.05%. Cluster 2 involves around 12% fine siltstone, 2.33% claystone, 0.27% carbonate, and no albite. The detrital fragment increases to 0.23%.

The total ratios of voxel porosity in each rock component over the three clusters are as follows: 0.29% detrital fragments, 50.74% fine siltstone, around 34% claystone, and 15% carbonate.

Albite has the lowest porosity ratio summation along with three clusters at 0.17% (Fig. 11).

Table 2 shows the means of voxel porosity for three clusters; the matrix cluster has a 3.39 mean value, whereas the macro-pores cluster has a 10.77 mean value and zero for the no-porosity cluster. Ratios of voxel-porosity of the three clusters have also been calculated and listed in Table 2; the matrix cluster forms 30.37%, the macro-pores cluster accounts for 14.65%, and the no-porosity cluster represents around 55% of the gross clusters' ratios.

The weighted porosity average of matrix and macro clusters in the full volume was calculated by multiplying the total voxel

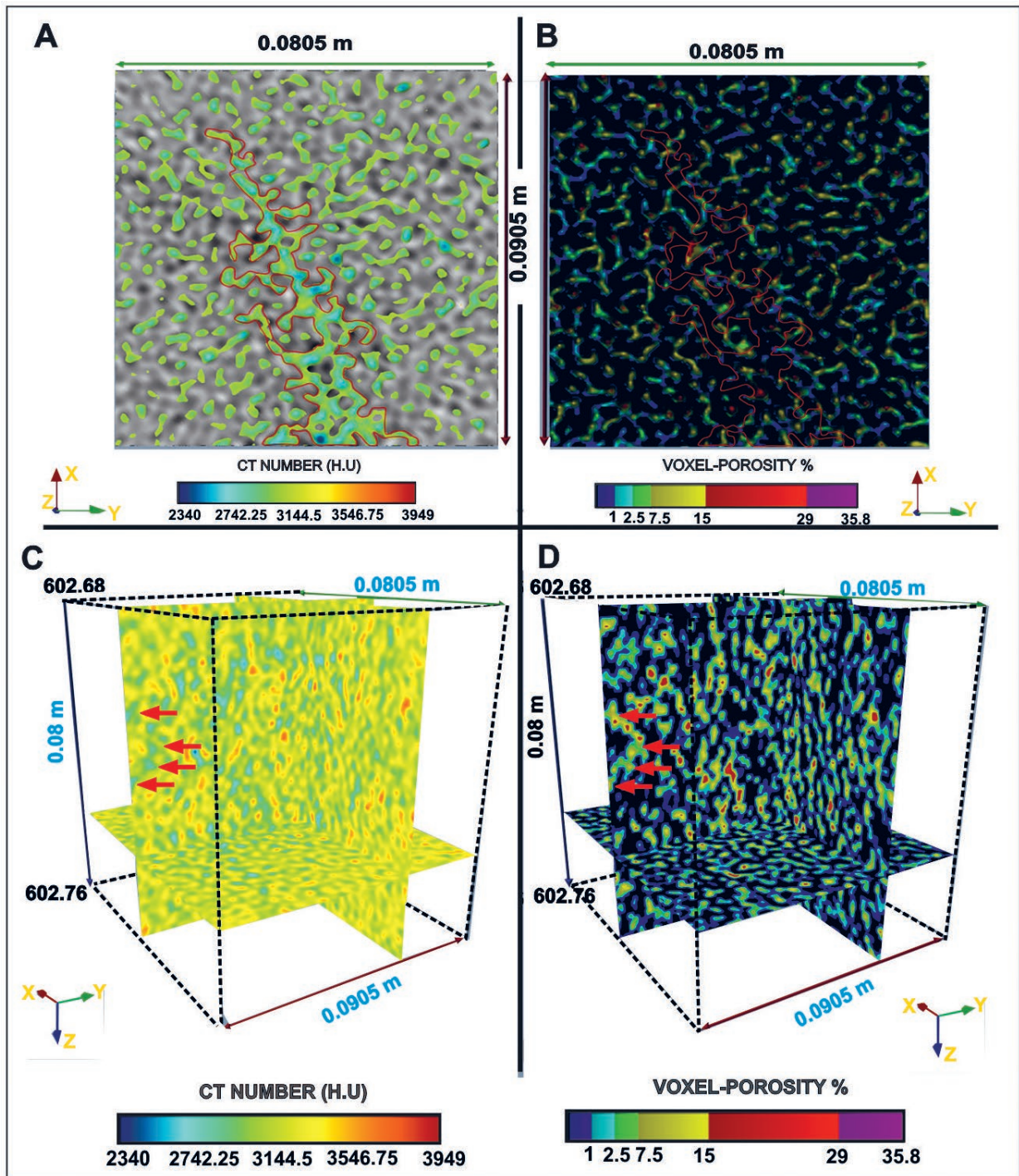


Figure 7. Fracture and convolute structures in the H.U. image and voxel-porosity slices. Red borders in A-B show a calcite filled fracture, whereas red arrows in C-D illustrate an example of a convolute structure in the detrital fragments and siltstone constituents.

Table 2. Comparison of mean porosity coming from CT scans with routine porosity measurements.

	Mean of voxel porosity where poro.>0 (C1)	No of voxels (%) C2	The ratio of voxels (%) C3	Porosity in the full volume (%)		
				From CT scans (C1*C3/100) for macro and matrix	He- porosity	Hg-porosity
Matrix	3.3	4035718	30.37	1.002	-	1.59
Macro-pores	10.77	1946183	14.65	1.578	-	-
Matrix and macro	5.72	5981901	45.02	2.575(*)	2.51	2.02
No-porosity	0	7306394	54.98	0	-	-

(*) weighted average

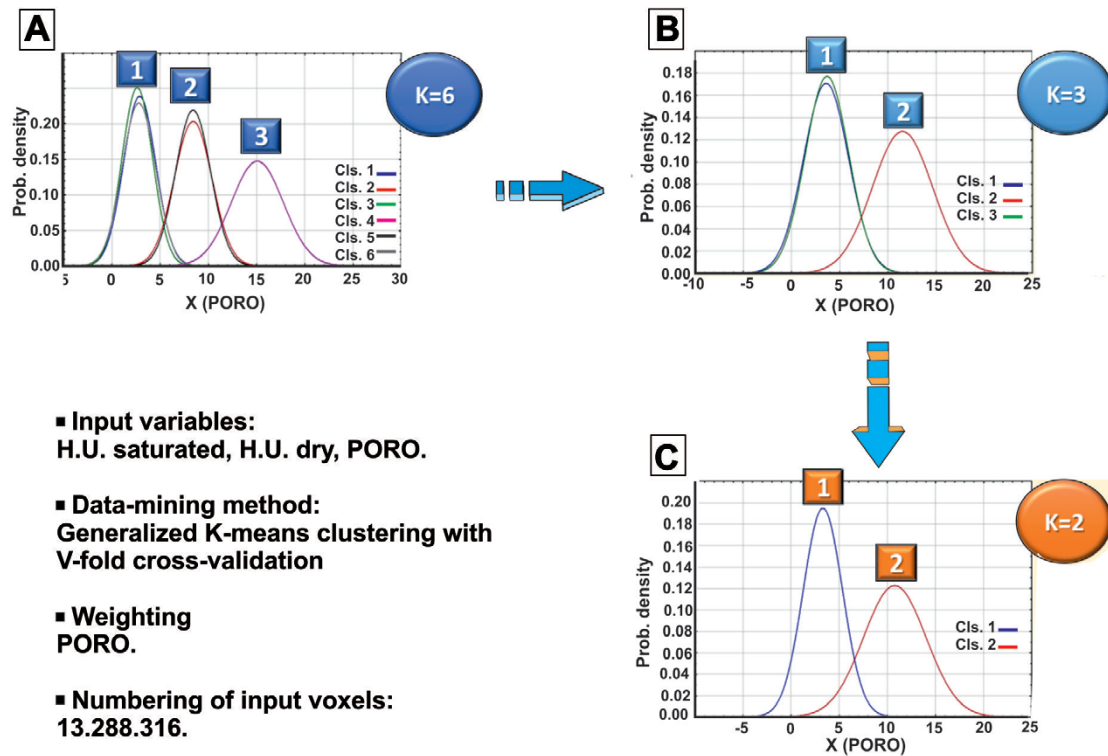


Figure 8. Sequence clustering of voxel-porosity values.

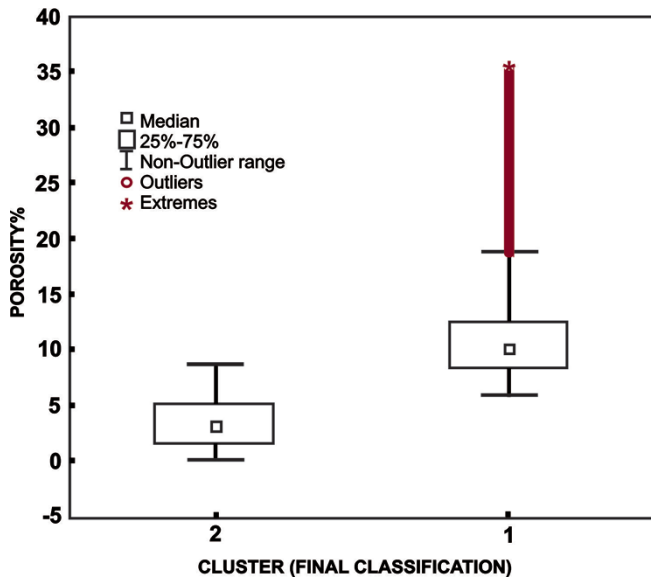


Figure 9. Box-plot of porosity by clusters; cluster 1 represents the macro-pores cluster, and cluster 2 refers to the Matrix cluster.

count (C1) for each cluster, by the ratio of voxel porosity of these clusters (C3). Results were arithmetically adding and resulted in a value of 2.58% (Table 1). The final average number reflects each observation's relative importance and is accordingly more descriptive than a simple average. In comparison, the He porosimetry measurements show quite close value for the calculated porosity mean of the CT scans image (2.51%) while the Hg measurement given smaller porosity mean values at 2.02%. More detailed data can be seen in Table 2. The Hg and He measurements were carried out in the GEOCHEM Laboratory and the results published in FEDOR et al., 2018.

6. DISCUSSION

The various illite and illite/smectite mixed assemblages represent the dominant clay minerals of the Boda claystone Formation (NÉMETH & MÁTHÉ, 2016). Clay minerals are present in the form of a detrital matrix or as part of rock fragments known as „alloctenic clays” as well as replacements (by alterations) or cement, called authigenic clays. Authigenic clay minerals impact formation porosity to a greater extent because of their direct vulnerability to pore fluids compared to detrital clay minerals, which are tightly packed in the rock matrix. Authigenic clay minerals occur as pore linings, pore fillings, pseudomorphic replacements, and fracture fillings (e.g. AHMAD et al., 2018). The reactions of water with these clay minerals (during the core sample's saturation phase) significantly impacted the petrophysical properties. These reactions cause dissolution, precipitation, plugging, clay swelling, and migration of fine particles. The porous medium of siltstone and detrital fragments can be represented as a network, consisting of pores connected by throats or narrower pore channels. The presence of clay minerals as a dispersed matrix in the pore space reduces the pore throat size and overall permeability due to the release of clay particles from pore walls and their subsequent redeposition downstream in the pore throats, which presumably results in plugging of the pore throats (AL-YASERI et al., 2015; HAYATDAVOUDI AND GHALAMBOR 1996; SIMON AND ANDERSON 1990; ZHOU et al. 1995).

The variations of the HU observations in Fig. 5A could be assigned to the release of fine grains of non-clay minerals (such as carbonate or albite cement) and clay particles (such as illite) from pore filling and subsequent redeposition downstream in pore throats of the fine siltstone component, otherwise dispersed in the original claystone structure. That could explain the relative decrease of the claystone and fine siltstone HU observations in Fig. 5A. Simultaneously, the migration of fines from the detrital

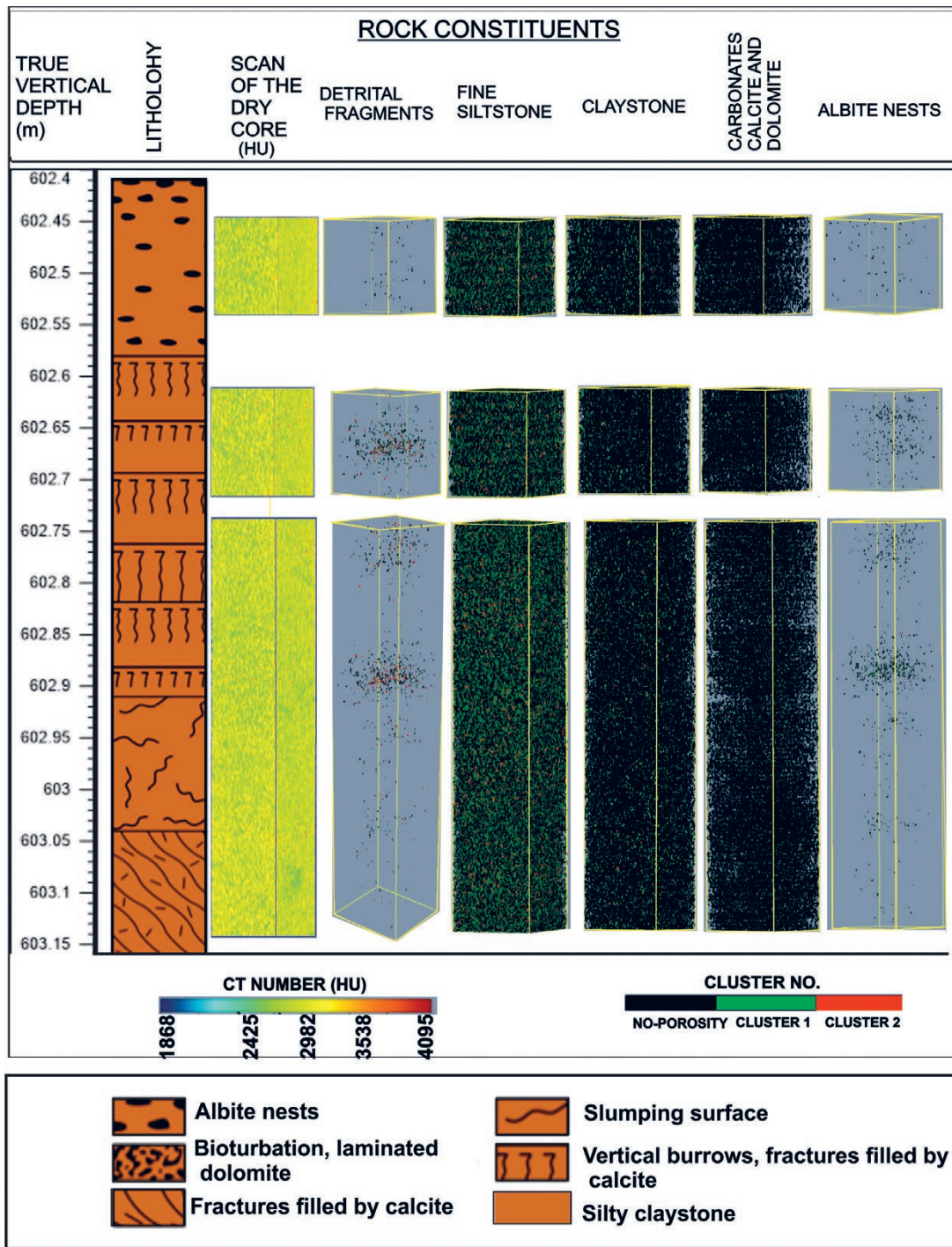


Figure 10. Porosity clusters by rock-forming components.

fragments within porous media could be seemingly the source of lesser representation of dispersed material and increased values of the saturated HU observations in Fig. 5A.

Swelling clays, such as smectite and mixed-layer clays, first expand under favourable ionic conditions and then disintegrate and migrate. Smectites can be significantly affected by minor changes in temperature and water vapour pressure, leading to changes in rock strength, porosity, and permeability. The reactions of concern include (1) reversible collapse/expansion of the smectite layers due to loss/gain of interlayer water; (2) irreversible collapse due to loss of interlayer water and migration of interlayer cations into the 2:1 silicate layers; (3) irreversible reduction of the

osmotic swelling ability through reaction in a steam atmosphere; and (4) inhomogeneous transformation of the smectite into an interstratified illite/smectite (PUSCH & KARNLAND, 1996).

Accordingly, three scenarios could be proposed to interpret outliers in Fig. 5B; non-swelling clays e.g., Kaolinites and illites, tend to detach from the rock surface, migrating (non-clay) fine particles e.g., cement, and smectite might swell and become free to move. These suggestions could explain the full or partial plugging of the pore throats and the increase of the minimum HU values outlier. Beyond that, collapsing of smectite, through one of the four above points, could lead to the adsorption of less water during the saturation phase, which together with particles re-

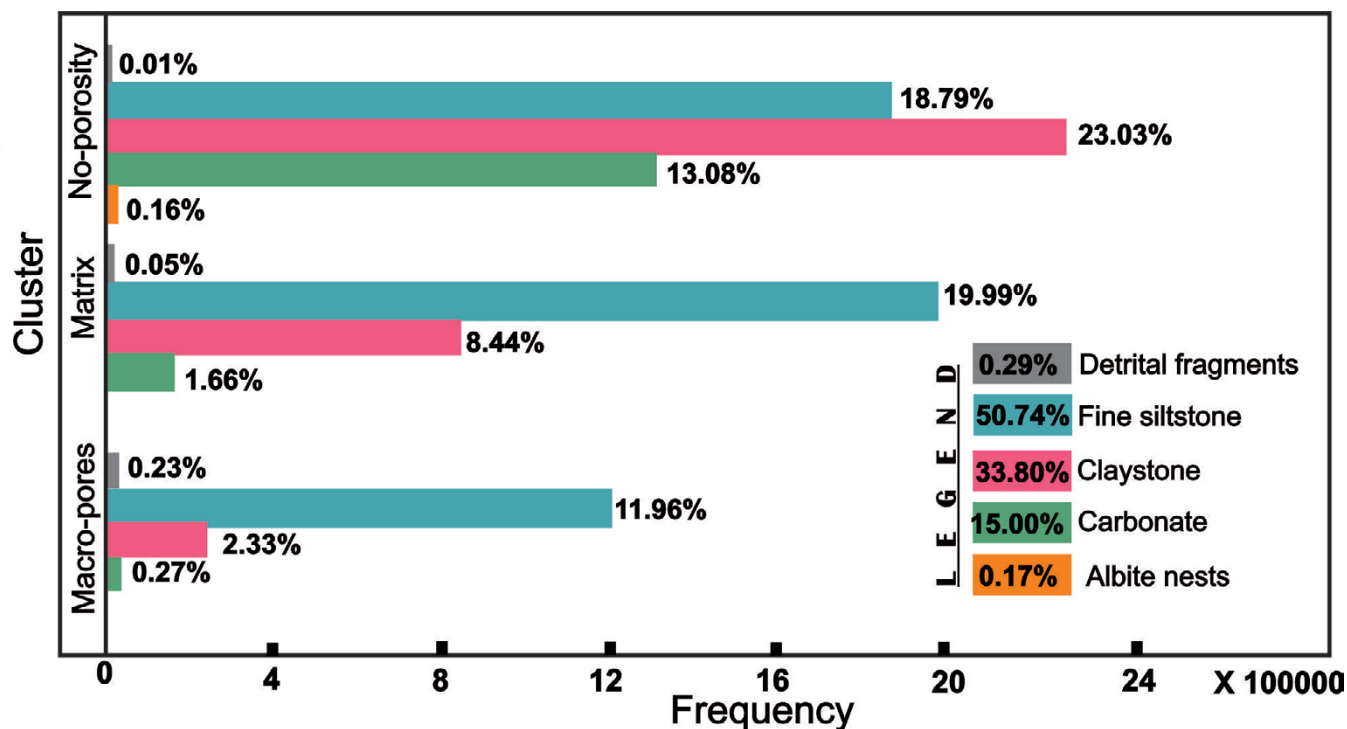


Figure 11. Crosstabulation chart table of rock components and clusters.

leasing from the detrital deposit structure could also create additional pore space. Appropriately, the maximum HU outlier in Fig. 5B and Fig. 9 would result.

The exceptionally high coefficient of variation percentage of the detrital terrigenous fragments constituent (1039.39%) in Table 1, reflects the high ratio of the standard deviation compared to the mean. The more extreme the outlier (32.33%), the more the standard deviation is affected, and the greater coefficient of variation arises. The large proportion of the minimum outlier probably results from migrating non-clay and/or non-swelling particles from pore walls during the flooding process. It could occur due to migration of smectite with the fluid flowing through the porous formation. In contrast, the fine siltstone coefficient of variation ratio is way lower than the detrital fragments variation (134.99%). This is relevant to the higher mean value (3.39%) and lower minimum porosity of outliers (15.14%). It could be said therefore that the lower the outlier ratio, the less the standard deviation is affected, and the smaller proportion of the variation coefficient produced. It is quite appropriate reliable to recall the throat plugging proposal here.

The low porosity outlier proportions of Claystone, carbonate, and albite seem not to affect the coefficient variation ratios. Relative high coefficients of variations have resulted from high standard deviation values comparable with low mean values. It is worthy to note that since these three last components are classified as filling material components or dispersible particles, the low minimum porosity outlier ratios are to be expected.

The descending porosity ratio of claystone accompanied by the lower carbonate porosity ratio over the three clusters in Fig. 11 seem to play a significant role in the porosity distribution of clusters. Comparing the claystone ratios across the three clusters; the no-porosity cluster has an extraordinary claystone proportion (around 23%), while the matrix and macro clusters show lower claystone ratios at 8.44% and 0.27%, respectively. Correspondingly, the carbonate cement has a high proportion in the no-po-

rosity cluster (about 19%), and it decreases in both the matrix (1.66%) and macro-pore (0.27%) clusters. This observation suggests the higher the claystone and carbonate ratios, the lower the porosity proportions. It is also highly expected to find authigenic clay in the claystone component of the no-porosity cluster (0.16%), whereas in the macro-pores cluster, albite is absent, and the detrital fragments occur instead (0.23%). It could be expected that pore spaces (macro-pores) might be created within the portion of the detrital fragment because of the larger relative grain size.

Claystone and carbonate components are reasonably consistent; reducing claystone across the three clusters is associated with a decreasing carbonate ratio while albite would not produce a similar result. The difference of coincidence between these three components is related to the BCF diagenetic phases. The weathered residue of the basement mafic rocks accounts for authigenic deposits in the BCF playa basin. Albite cement (Pore-filling and interstitial) is formed by adding Na ions from an alkaline brine and evaporites to the Boda claystone sediments. The formation of albite was the reason for the depletion of Na ions in the claystone. Ca and K-enriched waters reacted with smectite and kaolinite to yield K-rich illite with precipitation of Ca in carbonate cement (VARGA et al., 2005).

The Chi-square independence test emphasized that the clusters are related to their rock-type constituents at the 95% confidence level for a particular case. The Lambda and Pearson's R tests were applied to detect the association between clusters and rock-type variables. Based upon the Lambda value (0.0856), the reduction in error when a cluster is used to predict rock components is 8.56%. Also, Pearson's correlation shows a significant association between clusters and rock components at the 95% confidence level. The R-value was around 0.4.

The measurement protocol of the CT-laboratory allows a maximum of 10 HU absolute value noise. In the studied core, only

Table 3. Statistical characteristics of the density contrast between the dry and saturated scans and the calculated voxel porosity of the 10 HU absolute value noise.

	Valid N	Mean	Min.	Max.	Std.Dev
FLD-DRY (HU)	246187	5.501	1	10	2.869
Porosity (%)	246187	0.175	0.028	0.4	0.091

1.6% of the total number of voxels showed that the difference between the saturated and dry HUs was less than 10 HU. Table 3 shows the statistical characteristics of the density contrast between the dry and saturated scans and the calculated voxel porosity of this noisy-critical subset. The average mean of the difference between the saturated and dry HU values (<10 HU) was around 5. It can also be seen that the voxel porosity varies between 0.028 % and 0.40 % in this subset. The corresponding mean voxel-porosity is 0.17%. If we suppose that all HU contrast measured in this critical subgroup is noise, then the average voxel-porosity calculated for the whole core, 2.51%, can be decreased by a minimum of 0.028% porosity and a maximum of 0.40% porosity. So the average voxel porosity corrected by the expected noise may vary between 2.11% and 2.34%.

By neglecting the noise effect, the difference between the CT porosity scanned volume, and the mercury porosity means value in Table 2 is caused due to the limitation of mercury measurements. Small pore volumes are usually not accessed by the mercury, even at the highest pressures. Unreachable minute pores in the Hg method reduce the porosity mean to 2.02%, while the mean porosity of the CT scans is 2.57%. However, the helium molecule's small size enables its entrance into the narrow pore structures and penetration into even the smallest pores. So, it gives a similar value for the porosity mean as the scanned CT volume (2.51%).

The hypothesis testing has been executed to determine which laboratory pore measurements should be considered and which should be discarded. The null hypothesis assumed that the difference between the mean CT and Hg porosity values are equal to zero. As a result, the null hypothesis is rejected at the 95% confidence level, and the confidence interval shows that the values of (CT mean= Hg mean) supported by data fall between (0.272 and 0.827). In the mean CT and He values comparison, the null hypothesis could not be rejected since the confidence interval supported by the data falls between (-0.217 and 0.337). From this perspective, only the He measurement could be considered reliable.

7. SUMMARY

This work proposed a straightforward procedure to estimate the rocks' petrophysical properties of a selected core sample volume. The dual CT scans' parameters were analyzed to establish the direct relationship between the rock-forming components and the petrophysical properties. Voxel-porosity of the rock constituents was successfully classified into three major clusters based on porosity and textural patterns.

Two major pore regimes are demonstrated by the heterogeneous spatial distribution of pore volume; matrix porosity and Vug porosity. Micropores from the matrix cluster occupy a significant proportion of the total porosity. Authigenic minerals play an influential role in decreasing the pore volume and plugging the pore throats via the swelling and migration of fine particles. Obtained mean porosity value corresponds well with the mean porosity measured by helium porosimetry. The discrepancy be-

tween the mean CT porosity value and mean porosity value obtained by Hg measurements can be assigned to the limitations of the laboratory method with respect to inaccessibility of small pores to mercury penetration.

Cementation and the authigenic clay content are considered to be the main pore volume-controlling factors of the BCF core sample. However, sedimentary structures, i.e., convolute structures, could also be a significant porosity-improving factor.

ACKNOWLEDGEMENT

The authors would like to acknowledge the Public Limited Company for Radioactive Waste Management (PURAM) to permit the University of Szeged to use their data sets in its scientific research work.

This research is sponsored by; Interdisciplinary Excellence Centre, Institute of Geography and Earth Sciences, Long Environmental Changes Research Team, Grants 20391-3/2018/FEKUSTRAT and GINOP-2.3.2-15-2016-00009 'ICER' of the European Union and the State of Hungary, Ministry of Human Capacities. Mecsekérc Ltd had financed the measurements. Co-financing was provided by the European Regional Development Fund.

REFERENCES

- AHMAD, K.M., KRISTÁLY, F. & TURZO, Z. (2018): Effects of clay mineral and physico-chemical variables on sandstone rock permeability. – *J Oil Gas Petrochem Sci.*, 1/1, 18–26. doi:10.30881/jogps.00006
- AKIN, S., DEMIRAL, B. & OKANDAN, E. (1966): A Novel Method of Porosity Measurement Utilizing Computerized Tomography. – *In Situ*, 20/4, 347–365.
- AL-YASERI, A.Z., LEBEDEV, M., VOGT S.J., JOHNS, M.L., BARIFCANI, A. & IGLAUER, S. (2015): Pore-scale analysis of formation damage in Bentheimer sandstone with in-situ NMR and micro-computed tomography experiments. – *J. Petrol. Sci.*, 129, 48–57. doi: 10.1016/j.petrol.2015.01.018
- ARNS, C.H., KNACKSTEDT, M.A., PINCZEWSKI, W.V. & LINDQUIST, W.B. (2001): Accurate estimation of transport properties from microtomographic images. – *Geophysical Research Letters*, 28, 3361–3364. doi: 10.1029/2001GL012987
- ATTIX, F.H. (1986): *Introduction to Radiological Physics and Radiation Dosimetry.* – Wiley-VCH. doi: 10.1002/9783527617135
- BALÁZS, GY.L., LUBLÓY, É. & FÖLDES, T. (2018): Evaluation of Concrete Elements with X-Ray Computed Tomography. – *J. Mater. Civ. Eng.*, 30/9, 06018010. doi: 10.1061/(ASCE)MT.1943-5533.0002389
- BOGNER, P.T., FÖLDES, F. & ZÁVODA, I.R. (2003): Application of CT and MR in the carbon hydrogen research. – *J. Hongroise Radiology*, 77/5, 231–237.
- BONNER, B.P., ROBERTS, J.J. & SCHNEBERK, D.J. (1994): Determining water content and distribution in reservoir graywacke from the northeast Geysers with X-ray computed tomography. – *Geotherm. Resource Council Trans*, 18, 305–310.
- CNUDDÉ, V., MASSCHAELE, B., DIERICK, M., VLASSEN BROECK, J., VAN HOO-REBEKE, L. & JACOBS, P. (2006): Recent progress in X-ray CT as a geosciences tool. – *Applied Geochemistry*, 21/5, 826–832. doi: 10.1016/j.apgeochem.2006.02.010
- COKER, D.A., TORQUATO, S. & DUNSMUIR, J.H. (1996): Morphology and physical properties of Fontainebleau sandstone via a tomographic analysis. – *Journal of Geophysical Research*, 101, 17497–17506. doi: 10.1029/96JB00811
- COLES, M.E., HAZLETT, R.D., SPANNE, P., SOLL, W.E., MUEGGE, E.L. & JONES, K.W. (1998): Pore level imaging of fluid transport using synchrotron X-ray microtomography. – *Journal of Petroleum Science and Engineering*, 19/1–2, 55–63. doi: 10.1016/S0920-4105(97)00035-1
- COLES, M.E., MUEGGE, E.L. & SPRUNT, E.S. (1991): Applications of CAT scanning for oil and gas-production research. – *IEEE Transactions on Nuclear Science*, 38/2, 510–515. doi: 10.1109/NSSMIC.1990.693464
- CORMACK, A.M. & HOUNSFIELD G.N. (1989): *Physiology or medicine 1979: Press release.* Accessed April 21, 2018. https://www.nobelprize.org/nobel_prizes/medicine/laureates/1979/press.html.
- CSONTOS, L. & VÖRÖS, A. (2004): Mesozoic plate tectonic reconstruction of the Carpathian region. – *Palaeogeography, Palaeoclimatology, Palaeoecology*, 210/1, 1–56. doi: 10.1016/j.palaeo.2004.02.033
- FLANNERY, B.P., DECKMAN, H.W., ROBERGE, W.G. & D'AMICO, K.L. (1987): Three-dimensional X-ray microtomography. – *Science*, 237, 1439–1444. doi: 10.1126/science.237.4821.1439

- FEDOR, F., MÁTHÉ, Z., ÁCS, P. & KORONCZ, P. (2018): New results of Boda Claystone research - genesis, mineralogy, geochemistry, petrophysics.– In: NORRIS, S., NEEFT, E.A.C. & VAN GEET, M. (eds.): Multiple Roles of Clays in Radioactive Waste Confinement. Geological Society, London, Special Publications, 482, doi: 10.1144/SP482.13
- FÖLDES, T. (2011): Integrated processing based on CT measurement.– *J. News Geom.*, 1, 23–41.
- FÖLDES, T.B., KISS, G., ÁRGYELÁN, P., BOGNER, I. & REPA, K. HIPS. (2004): Application of medical computer tomography measurements in 3D reservoir characterization.– *Acta Geologica Hungarica*, 47/1, 63–73. doi: 10.1556/AGeol.47.2004.1.5.
- FREDRICH, J.T., GREAVES, R.H. & MARTIN, J.W. (1993): Pore geometry and transport properties of Fontainebleau sandstone.– *International Journal of Rock Mechanics & Mining Sciences & Geomechanics Abstracts*, 30, 691–697. doi: 10.1016/0148-9062(93)90007-Z
- GARVEY, C.J. & HANLON, R. (2002): Computed tomography in clinical practice.– *British Med. J.*, 324 /7345, 1077–1080. doi: 10.1136/bmj.324.7345.1077
- GEIGER, J., HUNYADFALVI, Z. & BOGNER, P. (2009): Analysis of small-scale heterogeneity in clastic rocks by using computerized X-ray tomography (CT).– *Eng. Geol.*, 103, 112–118. doi: 10.1016/j.enggeo.2008.06.011
- GUNTORO, P.I., GHORBANI, Y., KOCH, P.H. & ROSENKRANZ, J. (2019): X-ray Microcomputed Tomography (μ CT) for Mineral Characterization; A Review of Data Analysis Methods.– *Minerals*, 9, 183 p. doi: 10.3390/min9030183
- HAAS, J. & PÉRO, C.S. (2004): Mesozoic evolution of the Tisza Mega-unit.– *International Journal of Earth Sciences*, 93, 297–313.
- HAYATDAVOUDI, A. & GHALAMBOR, A. (1996): Controlling formation damage caused by kaolinite clay minerals: Part I.– In: SPE Formation Damage Control Symposium, Society of Petroleum Engineers, SPE-31118-MS. doi: 10.2118/31118-MS
- HOUNSFIELD, G.N. (1973): Computerized transverse axial scanning (tomography). 1. Description of system.– *Br. J. Radiol.*, 46/552, 1016–1022. doi: 10.1259/0007-1285-46-552-1016
- HOVE, A.O., NILSEN, V. & LEKNES, J. (1988): Visualization of Xanthan Flood Behavior in Core Samples by Means of X-Ray Tomography.– SPEJDOE, 17342.
- JONES, K.W., SPANNE, P., WEBB, S.W., CONNER, W.C., BEYERLEIN, R.A., REAGAN, W.J. & DAUTZENBERG, F.M. (1991): Catalyst Analysis using Synchrotron X-ray Microscopy.– *Nuc. Inst. Meth. Phys. Res.*, 56–57, 427–432. doi: 10.1016/0168-583X(91)90603-Q
- KNOLL, G.F. (2000): Radiation Detection and Measurement.– *J. Wiley & Sons.*, 816 p.
- KOCH, A., RAVEN, C., SPANNE, P. & SNIGIREVA, A. (1998): X-ray imaging with submicrometer resolution employing transparent luminescent screens.– *Journal of the Optical Society of America. A, Optics and Image Science*, 15/7, 1940–1951.
- KONRÁD, G.Y. (1999): The Boda Claystone Formation. The Geology of today for tomorrow.– *Excursion Guide Book (A satellite conference of the World Conference of Science, Budapest)*, 65–75.
- KONRÁD, G.Y., SEBE, K., HALÁSZ, A. & BABINSZKI, E. (2010): Sedimentology of a Permian playa lake: The Boda Claystone Formation, Hungary.– *Geologos*, 16, 27–41. doi: 10.2478/v10118-010-0002-1.
- LEDLEY, R.S., CHIRO, G.D., LUESSENHOP, A.J. & TWIGG, H.L. (1974): Computerized transaxial X-ray tomography of the human body.– *Science*, 186, 207–212.
- LONTOC-ROY, M., DUTILLEUL, P., PRASHER, S.O., HAN, L.W. & SMITH, D.L. (2005): Computed tomography scanning for three-dimensional imaging and complexity analysis of developing root systems.– *Canadian Journal of Botany*, 83, 1434–1442. doi: 10.1139/b05-118
- LOUIS, L., WONG, T. F. & BAUD, P. (2007): Imaging strain localization by X-ray radiography and digital image correlation: deformation bands in Rothbach sandstone.– *Journal of Structural Geology*, 29/1, 129–140. doi: 10.1016/j.jsg.2006.07.015
- MOSS, R.M., PEPIN, G.P. & DAVIS, L.A. (1990): Direct measurement of the constituent porosities in a dual porosity matrix.– *SCA conference*, 9003.
- NAHMANI, J., CAPOWIEZ, Y. & LAVELLE, P. (2005): Effects of metal pollution on soil macroinvertebrate burrow systems.– *Biology and Fertility of Soils*, 42, 31–39. doi: 10.1007/s00374-005-0865-4
- NÉMETH, T. & MÁTHÉ, Z. (2016): Clay mineralogy of the Boda Claystone Formation (Mecsek Mts., S.W. Hungary).– *Open Geoscience*, 8, 259–274. doi: 10.1515/geo-2016-0024.
- NICHOLS, M.C., KINNEY, J.H., JOHNSON, Q.C., SAROYAN, R.A., BONSE, U., NUSSHARDT, R. & PAHL, R. (1989): Synchrotron Microtomography of Supported Catalysts.– *Rev. Sci. Inst.*, 60/7, 2475. doi: 10.1063/1.1140703
- PURCELL, C., HARBERT, W., SOONG, Y., MCLENDON, TR, HALJASMAA, IV, MCINTYRE, D. & JIKICH, J. (2009): Velocity measurements in reservoir rock samples from the SACROC unit using various pore fluids, and integration into a seismic survey taken before and after a CO₂ sequestration flood.– In: GALE, J., HERZOG, H. & BRAITSCH, J. (eds.): Energy Procedia: Greenhouse Gas Control Technologies, 9, Elsevier Science, Amsterdam, 2323–2331. doi: 10.1016/j.egypro.2009.01.302
- PUSCH, R. & KARNLAND, O. (1996): Physico/chemical stability of smectite clays.– *Engineering Geology*, 41/1–4, 73–85. Doi: 10.1016/0013-7952(95)00027-5.
- PYRAKNOLTE, L.J., MONTEMAGNO, C.D. & NOLTE, D.D. (1997): Volumetric imaging of aperture distributions in connected fracture networks.– *Geophysical Research Letters*, 24/18, 2343–2346.
- RIBEIRO, J.L.B., LOPES, R.T., ANJOS, M.J., QUEIROZ NETO, J.C., BIANCO, L.C.B., CAMPOS, E.F. & D'ALMEIDA, A.R. (2007a): Study of performance with diverting agents in formation damage and return of permeability for unconsolidated sandstones using computed tomography.– In: 2006 IEEE Nuclear Science Symposium Conference Record. Ieee, San Diego, CA, 7,7p. doi: 10.1109/NS-SMIC.2006.356039
- SCHWARTZ, M.F., SAFFRAN, E.M., FINK, R.B., MYERS, J.L. & MARTIN, N. (1994): Mapping therapy: A treatment programme for agrammatism.– *Aprasiology*, 8/1, 19–54. doi: 10.1080/02687039408248639.
- SIEGBAHN, K. (1967): Alpha, beta, and gamma ray spectroscopy.– North-Holland, Amsterdam.
- SIMON, D. & ANDERSON, M. (1990): Stability of clay minerals in acid.– In: SPE Formation Damage Control Symposium. Society of Petroleum Engineers, SPE-19422-MS, doi: 10.2118/19422-MS
- SPANNE, P. & RIVERS, M. (1987): Computerized Microtomography using Synchrotron Radiation from the NSLS.– *Nucl. Instr. Meth. Phys. Res.*, 24–25, 1063, 67p. doi: 10.1016/S0168-583X(87)80312-9
- SPRUNT, E.S., DESAI, K.P., COLES, M.E., DAVIS, R.M. & MUEGGE, EL (1991): Cat Scan Monitored Electrical Resistivity Measurements Show Problems Achieving Homogeneous Saturation.– *Soc Pet. Eng.*, 21433.
- SUTTON, S.R., BERTSCH, P.M., NEWVILLE, M., RIVERS, M., LANZIROTTI, A. & ENG, P. (2002): Microfluorescence and microtomography analyses of heterogeneous earth and environmental materials.– In: FENTER, P., RIVERS, M., STURCHIO, N. & SUTTON, S. (eds.): Applications of Synchrotron Radiation in Low-Temperature Geochemistry and Environmental Sciences. Reviews in Mineralogy and Geochemistry, 49, 429–483. Doi: 10.1515/9781501508882-014
- VAN KAICK, G. & DELORME, S. (2005): Computed tomography in various fields outside medicine.– *European Radiology*, 15/S4, D74–D81. 10.1007/s10406-005-0138-1
- VARGA, A.R., SZAKMÁNY, GY., RAUCSIK, B. & MÁTHÉ, Z. (2005): Chemical composition, provenance and early diagenetic processes of playa lake deposits from the Boda Siltstone Formation (Upper Permian), SW Hungary.– *Acta Geologica Hungarica*, 48/1, 49–68. doi: 10.1556/AGeol.48.2005.1.2
- VERHELST, F., VERVOORT, A., DE BOSSCHER, P.H. & MARCHAL, G. (1995): X-ray computerized tomography: determination of heterogeneities in rock samples.– In: Proc. 8th Int. Congress of Rock Mechanics, ISRM/Balkema, 1,105–108.
- VINEGAR, H.J. & WELLINGTON, S.L. (1987): Tomographic imaging of three-phase flow experiments.– *The Review of Scientific Instruments*, 58/1, 96–107. doi: 10.1063/1.1139522
- VOZÁROVÁ, A., EBNER, F., KOVÁCS, S., KRÁUTNER, H-G., SZEDERKÉNYI, T., KRISTIĆ, B., SREMAC, J., ALJINOVIĆ, D., NOVAK, M. & SKABERNE, D. (2009): Late Variscan (Carboniferous to Permian) environments in the Circum Pannonian Region.– *Geologica Carpathica*, 60, 71–104.
- WENNBERG, O.P., RENNAN, L. & BASQUET, R. (2009): Computed tomography scan imaging of natural open fractures in a porous rock: geometry and fluid flow.– *Geophysical Prospecting*, 57 /2, 239–249. doi: 10.1111/j.1365-2478.2009.00784.x
- WESOLOWSKI, J.R. & H.M. LEV. (2005): CT: History, technology, and clinical aspects.– *Seminars in Ultrasound, CT and MRI*, 26/6, 376–379. doi: 10.1053/j.sult.2005.07.007
- WITHJACK, E.M. (1988): Computed tomography for rock property determination and fluid flow visualization.– *SPE Formation Evaluation*, 3/4, 696–704. doi: 10.2118/16951-PA
- YANG, Y., AYRAL, S. & GRYTE, C.C. (1984): Computer-Assisted Tomography for the Observation of Oil Displacement in Porous Media.– *Soc. Pet. Eng. J.*, 24/1, 53–55. doi: 10.2118/11758-PA
- ZHOU, Z., GUNTER, W. & JONASSON, R. (1995): Controlling formation damage using clay stabilizers: a review.– In: Annual Technical Meeting. Petroleum Society of Canada, PETSOC-95-71. doi: 10.2118/95-71